Materials Horizons

COMMUNICATION

View Article Online
View Journal | View Issue

Cite this: *Mater. Horiz.*, 2025, 12, 4274

Received 13th November 2024,
Accepted 14th March 2025

DOI: 10.1039/d4mh01625d

rsc.li/materials-horizons

Defect-engineered 2D Bi_2Se_3-based broadband optoelectronic synapses with ultralow energy consumption for neuromorphic computing†

Sanju Nandi,[a] Sirsendu Ghosal,[a] M. Meyyappan[b] and P. K. Giri *[ab]

Optoelectronic synapses (OES) inspired by the human brain have gained attention in addressing the von Neumann bottleneck facing traditional computing. Numerous candidates, including topological insulators and other 2D materials, have been used to fabricate OES devices with different degrees of success. Se vacancies commonly appearing in epitaxially grown Bi_2Se_3 and importantly the ability to modulate the vacancies by changing the growth temperature make it a worthy candidate to construct an OES system. The vacancies effectively trap and release charges, leading to persistent photoconductivity, which is the mechanism behind OES operation. A defect-induced Bi_2Se_3-based synapse using an ultrathin layer grown by chemical vapor deposition is shown herein to successfully demonstrate basic synapse characteristics such as paired-pulse facilitation (PPF), short-term and long-term memory, and learning–relearning behavior. This OES device shows a very high PPF index of 201.7%, a long memory retention time of 523.1 s, and an ultralow energy consumption of 9.2 fJ per spike, which is at the low end of the 1–100 fJ range for biological systems. Density functional theory simulations reinforce the definite role of trap centers induced by the Se vacancies in the device operation. Our device realizes a high recognition accuracy of 90.12% for MNIST handwritten digital images in simulations based on an artificial neural network algorithm. The exceptional results achieved here show the potential of Bi_2Se_3 for synaptic applications and pave the way for exploiting its potential in future high-performance neuromorphic computing and other artificial visual perception systems.

New concepts

Optoelectronic synapses (OES) are usually constructed using various mechanisms such as ionization and dissociation of oxygen vacancies in metal oxides, carrier capture and release by heterojunction barriers, defect-induced trapping and de-trapping, and others. Usually, 2D transition metal dichalcogenides exhibit intrinsic Se vacancy defects known to effectively trap and release charges, leading to persistent photoconductivity, a key mechanism in OES devices. Reliable operation of the devices with pre-designed characteristics requires control of the defects but it is an unaddressed challenge. Here, we demonstrate such defect engineering by controlling the growth temperature in the chemical vapor deposition of Bi_2Se_3. Devices with materials grown at low temperatures essentially behave as photodetectors due to the negligible presence of defects. As growth temperature increases, the increased density of Se vacancies leads to the desirable persistent photoconductivity, allowing the realization of OES devices based on 2D Bi_2Se_3. Besides such elegant control of defects, this work features an ultra-low power broadband OES system based on 2D Bi_2Se_3 for the first time, despite the material's significance in a wide range of other applications. The key metrics such as paired-pulse facilitation and energy consumption per spike achieved here are by far the best reported to date for single material based two-terminal devices. Rare exceptions reporting better performance involve complex heterostructures of multiple materials or three-terminal transistors. The mechanistic understanding behind the OES functionalities is gained from controlled experiments and density functional theory calculations on defect-rich 2D Bi_2Se_3.

Introduction

Artificial intelligence (AI) technology has garnered much attention recently in various applications starting from self-driving cars to robots in farming, healthcare, factories and automobiles.[1–3] Traditional separation of memory and processing units in the von Neumann computing system creates a bottleneck in meeting the demands of AI applications requiring high computing performance and energy efficiency.[4–6] This issue has led to significant efforts towards developing alternative architectures, among which, neuromorphic computing inspired by the human brain and based on artificial synapses is regarded as an effective strategy to address the shortcomings of the traditional computing architecture. A neuromorphic system offers advantages including the ability to perform simultaneous memory and logic processing, fast computing speeds, low power consumption, a high degree of parallelism and fault tolerance desired in executing perception, learning and memory tasks.[7]

---

[a] *Department of Physics, Indian Institute of Technology Guwahati, Guwahati 781039, India. E-mail: giri@iitg.ac.in*
[b] *Centre for Nanotechnology, Indian Institute of Technology Guwahati, Guwahati 781039, India*

† Electronic supplementary information (ESI) available. See DOI: https://doi.org/10.1039/d4mh01625d

While synaptic devices modulated by electrical signals[3,5] have been widely studied, the less explored optoelectronic synaptic (OES) devices offer advantages such as high bandwidth, low crosstalk, low power consumption and absence of R–C (resistance–capacitance) delay, making them better suited for building new generation computing systems.[8,9] Moreover, the human eye gathers over 80% of the information from intricate external surroundings.[10] Hence, the exploration of OES devices possessing flexibility and adaptability is significant in developing artificial visual perception systems. The field of optical information detection and processing has advanced significantly, leading to applications such as camera sensors, security systems, surveillance technologies, autonomous vehicles and biomedical imaging. Conventional integrated optical communication systems comprising photodetectors and von-Neumann processors face challenges of slow data transfer and high-power consumption due to separate memory and processing units, as mentioned earlier. OES devices, combining photo-detection and synaptic functions in one, are promising candidates as they directly respond to light stimulus, convert it into electrical current and enable real-time optical data processing creating temporary memory.[10,11] Hence, OES devices are capable of not only detecting light signals but also tracking their history, including parameters such as light wavelength and intensity, as well as the number, duration, and frequency of light pulses.

Several materials, including Si,[12] metal oxides (ZnO,[13] TiO_2,[14] VO_2,[10] and WO_3[15]), 2D metal chalcogenides (MoS_2,[16] WS_2,[17] $MoSe_2$,[18] WSe_2,[19] $PdSe_2$,[20] ReS_2,[21] and In_2Se_3[22]), oxychalcogenides (Bi_2O_2Se[23]), perovskites ($CsPbBr_3$,[24] $CsPbCl_3$,[25] and $(BA)_2PbI_4$[11]) and carbon materials (graphene[26] and MXenes[27]) have been utilized to construct OES devices for neuromorphic computing systems. All these candidates have their own advantages along with limitations. For example, metal oxide-based OES devices primarily operate within the UV region, while perovskites lack stability under atmospheric conditions. Metal chalcogenides exhibit low photocurrent under infrared light illumination, impeding their efficacy for broadband applications. Most devices reported in the literature in general feature a low PPF index, low retention time, and high energy consumption (the picojoule to even nanojoule range) compared to biological synapses (1–100 fJ[24]). Thus, a pressing demand exists to investigate other 2D material candidates capable of overcoming these limitations and delivering enhanced capabilities for OES applications.

Topological insulators (TIs) with narrow band gaps in the near to mid-infrared range have emerged as an excellent choice for constructing new-generation optoelectronic devices.[28–31] Bi_2Se_3 exhibits a bulk bandgap of 0.3 eV and a single Dirac cone in its surface states.[28,29] However, the surface states vanish for ultrathin Bi_2Se_3 (thickness <6 nm), making it a low bandgap semiconductor,[30] which allows it to absorb light across a wide spectral range. Additionally, it displays many desirable optoelectronic properties, including thickness-dependent optical absorption, tunable bandgap and polarization-sensitive photocurrent.[31,32] Intrinsic Se vacancy defects introduced during the growth of WSe_2,[19] $MoSe_2$,[18] $PdSe_2$[20] and Bi_2O_2Se[23] have been shown to effectively trap and release charges, leading to persistent photoconductivity, a key mechanism in OES devices. These Se vacancies are also quite common in ultrathin Bi_2Se_3,[31,33] thus indicating their potential for constructing OES devices, but this has not been explored to date. Wang *et al.* fabricated an OES device using an $MoSe_2/Bi_2Se_3$ hybrid in the visible to NIR range.[34] However, there is no report on only 2D Bi_2Se_3-based OES devices. Wan *et al.* used a similar TI material, Sb_2Te_3, to fabricate a simple two-terminal device showing OES characteristics.[35]

OES devices rely on mechanisms such as ionization and dissociation of oxygen vacancies in metal oxides, carrier capture and release by heterojunction barriers, defect-induced trapping and de-trapping, and others. As mentioned above, topological insulators exhibit intrinsic vacancy defects useful for the defect-mediated mechanism; however, control of the defects is critical for reliable device operation, which is the focus of this work. Interestingly, the growth of Bi_2Se_3 by any of the epitaxial techniques is amenable to controlling the defects at the growth stage itself by tuning the growth parameters (most ideally temperature), which is easier and preferable to other post-growth processes such as plasma treatment.[36] The latter becomes a useful option, in addition to other post-treatments, such as doping and annealing, in the case of films prepared by other techniques.

An OES device based on an ultrathin Bi_2Se_3 film grown by chemical vapor deposition (CVD) is demonstrated here. Se vacancies are induced and modulated in the Bi_2Se_3 film by varying the growth temperature. We have explored for the first time the optoelectronic characteristics of an only Bi_2Se_3 ultrathin film-based two terminal OES device for mimicking the rudimentary operations of a biological synapse. Typical optical synaptic behaviors, including paired-pulse facilitation (PPF), short-term memory (STM), long-term memory (LTM), and learning–relearning behaviors, were investigated by applying a train of light pulses. The fabricated device exhibits an excellent PPF index of 201.7% and a memory retention time of 523.1 s. The energy consumption per spike for the synaptic operation is 9.2 fJ, demonstrating very low energy consumption. The intrinsic Se vacancy defects in the Bi_2Se_3 crystal structure led to persistent photoconductivity, which has aided in formulating the artificial OES device. The observed performance is confirmed to be related to the Se vacancy defects of Bi_2Se_3 using density functional theory (DFT) calculations. An artificial neural network (ANN) architecture is simulated using the learning properties of our OES device to successfully realize a high recognition accuracy of 90.12% for MNIST (Modified National Institute of Standards and Technology) dataset handwritten digital images. The results of this study pave the way for fabricating future optical synaptic devices based on Bi_2Se_3, pointing to increased opportunities in the study of neuromorphic computing and artificial vision systems.

Experiments and modeling

Growth of Bi_2Se_3 ultra-thin films

Ultrathin 2D Bi_2Se_3 films were synthesized by CVD on a SiO_2/Si substrate (300 nm SiO_2 on Si) using a horizontal 30 mm diameter quartz tube furnace, as illustrated in Fig. S1 (ESI†). A high-purity Bi_2Se_3 powder (Alfa Aesar, 99.999%, 5 mg) precursor was placed in the middle of the CVD reactor. The SiO_2/Si substrate was placed 20–22 cm away from the center. A base pressure of 0.02 mbar was used, followed by multiple purges with argon to remove any moisture and oxygen contaminants. The temperature of the precursor was varied from 500 to 600 °C to investigate the effect of the precursor temperature on OES device performance. The furnace was heated to the desired temperature at a 15 °C per minute rate to initiate the growth process. The set temperature was held for an hour with an Ar flow at 165 standard cubic centimeters per minute (sccm). The pressure was maintained at 0.78 mbar during the growth. The substrate temperatures were 291, 314 and 335 °C for the three different precursor temperatures (500, 550 and 600 °C), respectively. The furnace was cooled naturally to room temperature after the growth. Consequently, large-area ultrathin 2D Bi_2Se_3 films were successfully synthesized on the SiO_2 substrate and extracted for further studies. The samples with different growth temperatures are denoted as BS1, BS2, and BS3, respectively, for precursor temperatures 500, 550, and 600 °C.

Device fabrication

The Bi_2Se_3-based optoelectronic artificial synapse device was fabricated by depositing gold (Au) electrodes on the ultrathin Bi_2Se_3 film. Here, we chose to construct a simple two-terminal device since it involves a less complex process compared to three-terminal transistor-like structures.[8,9,17,25] A mechanical mask was attached first to the film prior to metal deposition in order to define the electrodes and then Au was deposited onto the exposed areas of the film by a thermal evaporator ensuring precise and uniform electrode formation. The mechanical mask was removed after deposition, leaving behind a well-defined fabricated device with Au contacts on the Bi_2Se_3 film. The devices were annealed at 100 °C on a hotplate for 30 minutes after the deposition of the Au electrodes to improve the quality of the electrical contacts. This annealing step helps to enhance the adhesion between the gold electrodes and the Bi_2Se_3 film, ensuring better mechanical stability and electrical contact.

Characterization

X-ray diffraction (XRD, Rigaku RINT 2500 TTRAX – III s Cu K_α radiation) and micro-Raman spectroscopy (LabRam HR800, Jobin Yvon) were conducted to assess the crystallinity and phase of the as-grown Bi_2Se_3 films. We used a 532 nm laser to acquire the Raman spectra. The acquisition time was set to 15 s for all samples with a grating of 1800 grooves per mm. All measurements were conducted using a 100× (Olympus, N.A. 0.90) short working distance objective. A JEM 2100F microscope operating at 200 kV was used for field emission transmission electron microscopy (FETEM) to conduct an in-depth examination of the crystal structure, incorporating high-resolution TEM (HRTEM) analysis. X-ray photoelectron spectroscopy (XPS) measurements were performed with a PHI 5000 Versa Probe III (ULVAC – PHI, INC) to evaluate the composition and chemical states of the elements. The elemental compositions of the as-grown films were analyzed using a field emission scanning electron microscope (FESEM, Sigma, Zeiss) equipped with an energy-dispersive X-ray (EDX) spectrometer. The height profile of the as-grown thin films was measured using atomic force microscopy (AFM, Cypher, Oxford). The optical absorption of the films was investigated using a PerkinElmer LAMDA 950 UV-vis-NIR spectrometer. The electrical characteristics of the OES device, including current–voltage (*I–V*) characteristics and photoresponse, were studied using a microprobe station (ECOPIA EPS-500) with various lasers at different wavelengths (405 nm, 532 nm, 660 nm, and 808 nm). The laser diameter here is 1 mm. *I–V* measurements were made using a Keithley 4200 *I–V* measurement system and TTL (Transistor–Transistor Logic) modulation of a CNI laser.

DFT simulation

Density functional theory (DFT) calculations were carried out using a plane wave basis set in Quantum Espresso software[37,38] to obtain the density of states (DOS) as well as the electronic band structure. A $4 \times 4 \times 1$ supercell was constructed with 10 Å of a vacuum layer added in the *z* direction for both the pristine 4-layer Bi_2Se_3 and the defective structure, and a Monkhorst–Pack *k* point sampling of $12 \times 12 \times 2$ was used for sampling the Brillouin zone. The plane wave cut-off energy was set at 80 Ry, and an energy convergence threshold of 1×10^{-6} was kept to ensure the accuracy of the results. A force convergence cut-off value of 0.0001 eV $Å^{-1}$ was employed to achieve self-consistency. Projector-augmented-wave (PAW) pseudopotentials were used to describe the core electrons while the exchange–correlation potential was estimated using the generalized gradient approximation (GGA) with the Perdew–Burke–Ernzerhof (PBE) functional.[39,40] For the defective structure, 10% Se vacancies were created from several random spots in the supercell and then relaxed.

Results and discussion

Characterization of the 2D Bi_2Se_3 film

Fig. 1(a) presents the X-ray diffraction (XRD) patterns of as-grown Bi_2Se_3 films synthesized at different growth temperatures. The diffraction peaks observed for BS1 at 9.2°, 18.64°, 27.94°, 37.72°, 47.68°, and 57.76° correspond to the (003), (006), (009), (0012), (0015), and (0018) crystal planes of Bi_2Se_3. The peak positions for BS2 and BS3 are 9.22°, 18.7°, 28.02°, 37.9°, 47.88°, 57.7°, and 9.2°, 18.68°, 27.96°, 37.8°, 47.7°, 57.5°, respectively. These peaks align well with the standard values provided in the JCPDS card no. 33-0214, confirming the rhombohedral crystal symmetry of the as-grown Bi_2Se_3 films, which belong to the $R\bar{3}m$ space group.[41] The presence of only (00*n*) (*n* = 3, 6, 9, 12, 15, 18) diffraction peaks in the XRD patterns indicates that the Bi_2Se_3 films predominantly grow along the *c*-axis. Fig. S2a (ESI†) shows the fitted (006) peak of the XRD pattern. A shift of the (006) peak towards higher angles from BS1 to BS3 suggests a reduction in interplanar spacing (*d*-value), attributed to compressive strain induced by increasing

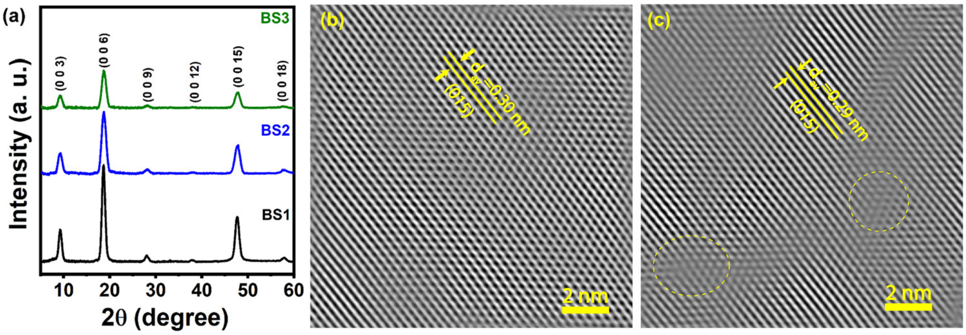

Fig. 1 (a) XRD pattern of the as-grown Bi_2Se_3 films BS1, BS2 and BS3 showing good crystallinity. (b) IFFT pattern of the HRTEM images of the BS1 sample showing high crystallinity. (c) IFFT pattern of the HRTEM image of the BS3 sample showing the lattice strain (encircled region).

growth temperature. Additionally, the full width at half maximum (FWHM) of the (006) peak increases from 0.82° (BS1) to 1.08° (BS3), as shown in Fig S2b (ESI†), indicating a decrease in crystallinity. The shift towards higher angles, along with reduced crystallinity in BS3 compared to BS1, suggests greater structural deformation and disorder, likely caused by changes in the Bi–Se bond distance due to surface Se vacancies.[42,43]

TEM analysis of BS1 and BS3 samples was conducted to examine their crystal structures further. Fig. S3a and b (ESI†) present the HRTEM images of BS1 and BS3, respectively. A closer look at the inverse fast Fourier transform (IFFT) patterns of these samples is provided in Fig. 1(b) and (c). The IFFT pattern of BS1 reveals well-defined crystalline lattice fringes characteristic of Bi_2Se_3, with an estimated *d*-spacing of approximately 0.30 nm, corresponding to the (015) plane of its rhombohedral crystal structure.[42] In contrast, the IFFT pattern of BS3 highlights the strain present in the sample, marked by an oval-shaped ring. The *d*-spacing in this strained region is around 0.29 nm, indicating compressive strain, which is also supported by XRD analysis. These lattice distortions could be attributed to Se vacancy defects in Bi_2Se_3.

Fig. 2(a) shows the Raman spectrum of the as-grown Bi_2Se_3 films at different temperatures. The Raman spectrum of BS1 shows three distinct peaks at 71.9, 132.2, and 175.0 cm^{-1}, which correspond to the A^1_{1g}, E^2_g and A^2_{1g} vibration modes, respectively. Here, A^1_{1g} and A^2_{1g} represent out-of-plane vibrations while E^2_g corresponds to the in-plane vibrations. The peak positions for BS2 and BS3 are at 71.5, 131.0, 174.8 cm^{-1} and 70.8, 129.8, and 175.1 cm^{-1}, which are consistent with previous reports confirming the high crystallinity of the CVD-grown Bi_2Se_3 ultrathin film.[32,41] The E^2_g mode peak positions display a slight redshift when increasing the growth temperature. The small shift in the Raman peak positions can be attributed to the increase in Se vacancies with the growth temperature.[44] Raman spectra of all the samples have been fitted as shown in Fig. S4a (ESI†), and the full width at half maximum (FWHM) of the A^1_{1g} modes has been compared with that of the bulk material (Fig. S4b, ESI†). The bulk precursor exhibits an FWHM of 3.3 cm^{-1}, while the values for BS1, BS2, and BS3 are 4.5 cm^{-1}, 4.6 cm^{-1}, and 4.9 cm^{-1}, respectively, all of which are comparable to the bulk, indicating good crystallinity. The FWHM increases systematically with increasing defect concentrations, as expected.

The elemental analysis and the valence states of elements in BS1, BS2 and BS3 were investigated by XPS. Fig. S5 (ESI†) shows the survey spectra of BS1, BS2 and BS3 confirming the presence of the Bi and Se elements. The peaks corresponding to Si and O are due to the SiO_2 substrate. XPS spectra of Bi 4f and Se 3d are shown in Fig. 2(b) and (c), respectively, for the as-grown Bi_2Se_3 films. Two prominent and separate peaks are observed in the Bi 4f spectrum of BS1 at binding energies of 158.0 eV and 163.3 eV, corresponding to Bi $4f_{7/2}$ and Bi $4f_{5/2}$, respectively. These peaks signify the Bi(III) valence state in Bi_2Se_3.[41,45] The peak positions in the case of BS2 and BS3 are 157.8 eV, 163.1 eV and 157.6 eV, 162.9 eV respectively. Similarly, the Se 3d spectrum of BS1 displays two well-fitted peaks at binding energies of 53.4 eV and 54.3 eV, corresponding to the Se $3d_{5/2}$ and Se $3d_{3/2}$ states, respectively. These peaks are characteristic of the Se(II) valence state.[41,45] The peak positions in the case of BS2 and BS3 are 53.3 eV, 54.2 eV and 53.1 eV, 54.0 eV respectively. The shift in both Bi 4f and Se 3d peaks towards lower binding energies while going from BS1 to BS2 to BS3 can be ascribed to the increase in Se vacancies.[42,46] Furthermore, weak peaks are observed at binding energies of 159.3 eV and 164.6 eV in the Bi 4f spectrum of BS3 in the tail region, which can be attributed to the presence of Bi–O bonds.[41]

A large number of Se atoms become exposed as the layer number of Bi_2Se_3 decreases and may separate from the surface, resulting in an abundance of Se vacancies in the 2D Bi_2Se_3 film. The presence of a large concentration of Se vacancies during growth at high growth temperature has been previously reported.[44,47] Moreover, Se has a lower electronegativity than oxygen, meaning that it takes less binding energy to break the Bi–Se bond as the number of vacancies rises. When the sample is exposed to air, atmospheric oxygen replaces the Se vacancies and creates a Bi–O bond.[33,48] The Se to Bi ratio can be calculated using the curve fitted inside the XPS spectra. The following relation was used to determine the Se to Bi ratio:[49]

$$\frac{\mathrm{Se}}{\mathrm{Bi}} = \frac{\dfrac{A_{\mathrm{Se}_{5/2}}}{S_{\nu(\mathrm{Se}_{5/2})}} + \dfrac{A_{\mathrm{Se}_{3/2}}}{S_{\nu(\mathrm{Se}_{3/2})}}}{\dfrac{A_{\mathrm{Bi}_{7/2}}}{S_{\nu(\mathrm{Bi}_{5/2})}} + \dfrac{A_{\mathrm{Bi}_{5/2}}}{S_{\nu(\mathrm{Bi}_{5/2})}}} \tag{1}$$

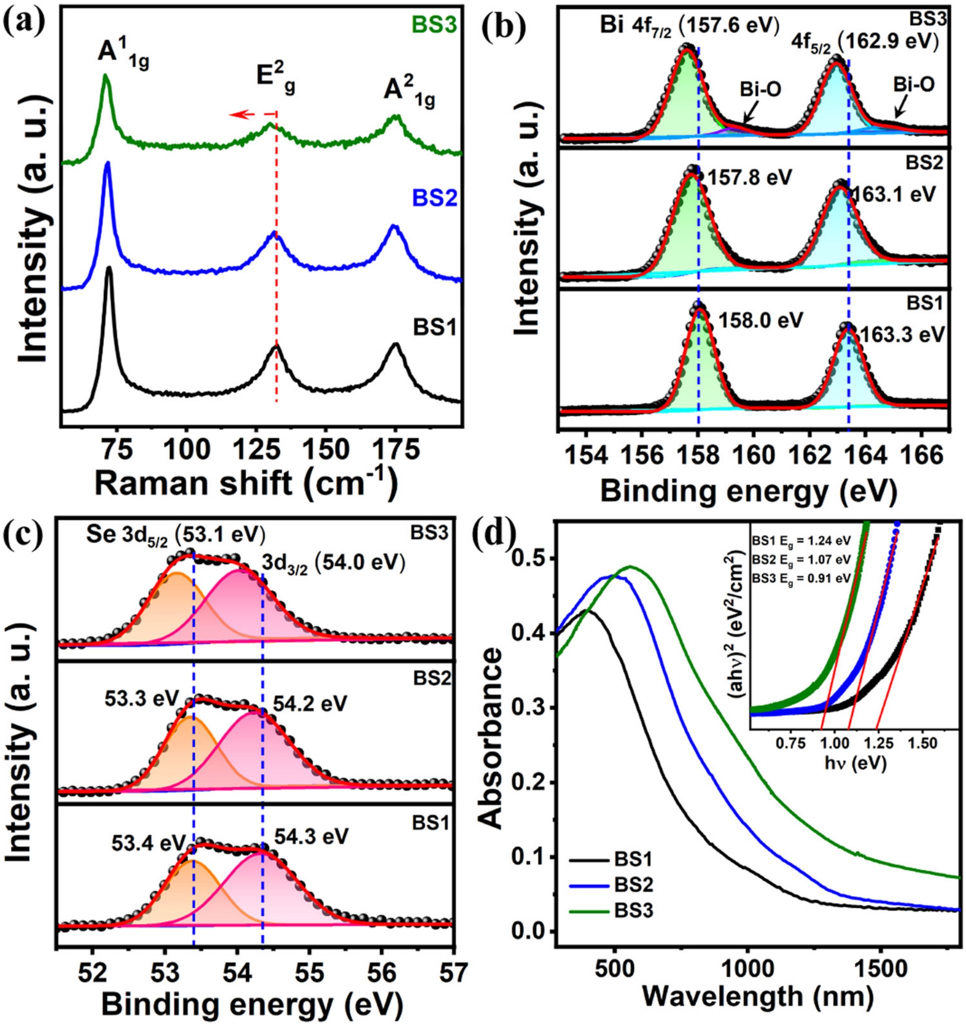

Fig. 2 (a) Raman spectra of the Bi_2Se_3 films (BS1, BS2, and BS3) showing characteristic Raman modes. (b) High-resolution XPS spectra of Bi 4f of the Bi_2Se_3 films (BS1, BS2 and BS3). (c) High-resolution XPS spectra of Se 3d of the Bi_2Se_3 films (BS1, BS2, and BS3). (d) Absorption spectra of the Bi_2Se_3 films (BS1, BS2, and BS3); the inset shows the calculated bandgaps of the films from the Tauc plot.

where A_x is the area under the fitted curve for the x-orbital and $S_{\nu x}$ is the corresponding sensitivity factor. The calculated ratios of Se/Bi for BS1, BS2, and BS3 are 1.49, 1.43, and 1.33, respectively, which confirms the increase in Se vacancies in the Bi_2Se_3 film with growth temperature. This behavior was also confirmed by energy-dispersive X-ray spectroscopy (EDS) as illustrated in Fig. S6 (ESI†), and the ratio of Se/Bi for BS1, BS2, and BS3 is found to be 1.47, 1.35 and 1.23 respectively. Fig. S7a–c (ESI†) show the AFM images taken at the film edges of BS1, BS2 and BS3. The thicknesses are found to be 4.11 nm, 3.92 nm, and 3.86 nm for BS1, BS2 and BS3, respectively, from the AFM height analysis shown in Fig. S7d–f (ESI†) corresponding to 4 quintuple layers (QL) of Bi_2Se_3 (1 QL = 0.95 nm). AFM analysis also confirms that the thickness of the films does not change much with growth temperature.

Fig. 2(d) displays the absorption spectrum of the three Bi_2Se_3 films on a sapphire substrate. The optical band gaps (E_g) of the as-grown Bi_2Se_3 thin films were determined by extending the Tauc plot's straight line, *i.e.* $(\alpha h\nu)^2$ *vs.* $h\nu$, as shown in the inset of Fig. 2(d) using the direct band gap semiconductor relation:

$$(\alpha h\nu)^2 = A(h\nu - E_g) \qquad (2)$$

where α is the optical absorption coefficient, $h\nu$ is the photon energy, and A is a constant. The estimated optical band gaps of BS1, BS2 and BS3 are 1.24 eV, 1.07 eV and 0.91 eV respectively, which are much greater than that of bulk Bi_2Se_3. The optical band gap value of Bi_2Se_3 is dependent on several factors including thickness, surface characteristics, morphology and synthesis methods.[50] Suitable tailoring of these parameters can lead to the quantum confinement effect along different directions. Bi_2Se_3 has an exciton Bohr radius of 21.79 nm, which is much higher than the film thickness ($\sim$4 nm) here.[51] Consequently, a wider optical bandgap is produced by quantum confinement resulting from the decreased thickness. Moreover, the reduction of bandgap with increase of growth temperature can be attributed to the increase in defect levels (Se vacancies here).

Light response characteristics of the OES device

Fig. 3(a) depicts a schematic of neurons and how signal transmission occurs across a synapse. Transmission of nerve impulses proceeds from one neuron to another *via* synapses, the junctions between neurons. Message transmission at the synapse occurs from one neuron to the post-synapse, possibly making the next neuron trigger its action potential.[52] Neurotransmitters are released during this process from the stimulated pre-synaptic neuron to the post-synaptic neuron, and the current of the post-synaptic neuron is determined by the neurotransmitter concentration. The intensity or amplitude of connections between neurons, which is the "weight" of a synapse, typically varies in response to a brain activity denoted as synaptic plasticity.[53] A parallel can be drawn between a biological synapse and a synaptic device: the alteration in the synaptic weight of the biological synapse is comparable to some specific parameter change such as resistance or conductivity in the synaptic device. Measuring the current across the optical synaptic device then is a practical approach to investigate the simulation of synaptic functions upon light activation. The current in the device, when exposed to light spikes, is referred to as the excitatory postsynaptic current (EPSC).

Fig. 3(b) shows a schematic of the constructed two-terminal OES device, which incorporates an ultrathin Bi_2Se_3 film as the functional layer along with two Au electrodes. A light stimulus serves as a presynaptic spike in this device, generating an EPSC within the Bi_2Se_3 channel. Fig. S8 (ESI†) shows the optical microscopy image of the fabricated OES device with two Au electrodes. The current–voltage (*I*–*V*) characteristics of all three devices under dark and illuminated (532 nm) conditions are examined first. Fig. S9a–c (ESI†) show the back-scanning *I*–*V* curves for the three devices BS1, BS2 and BS3 respectively. All the devices show increment in current under light illumination. Interestingly, hysteric *I*–*V* characteristics were observed in BS2 and BS3 samples. The current increases when the bias is swept from 5 V to 0 V just after the normal sweep of 0 to 5 V, which is due to the persistent photoconductivity in BS2 and BS3. This effect is more prominent in BS3 as expected since it has more Se vacancies.

Fig. 3(c) presents the transient optical response of the devices subjected to a single light pulse of 10 s of 532 nm laser with an intensity of 30.2 mW cm^{-2}. The device made of BS1 shows photodetector-like characteristics as it has no or very small number of defects. The long decay time for the current after removing the light pulse in the case of BS2 and

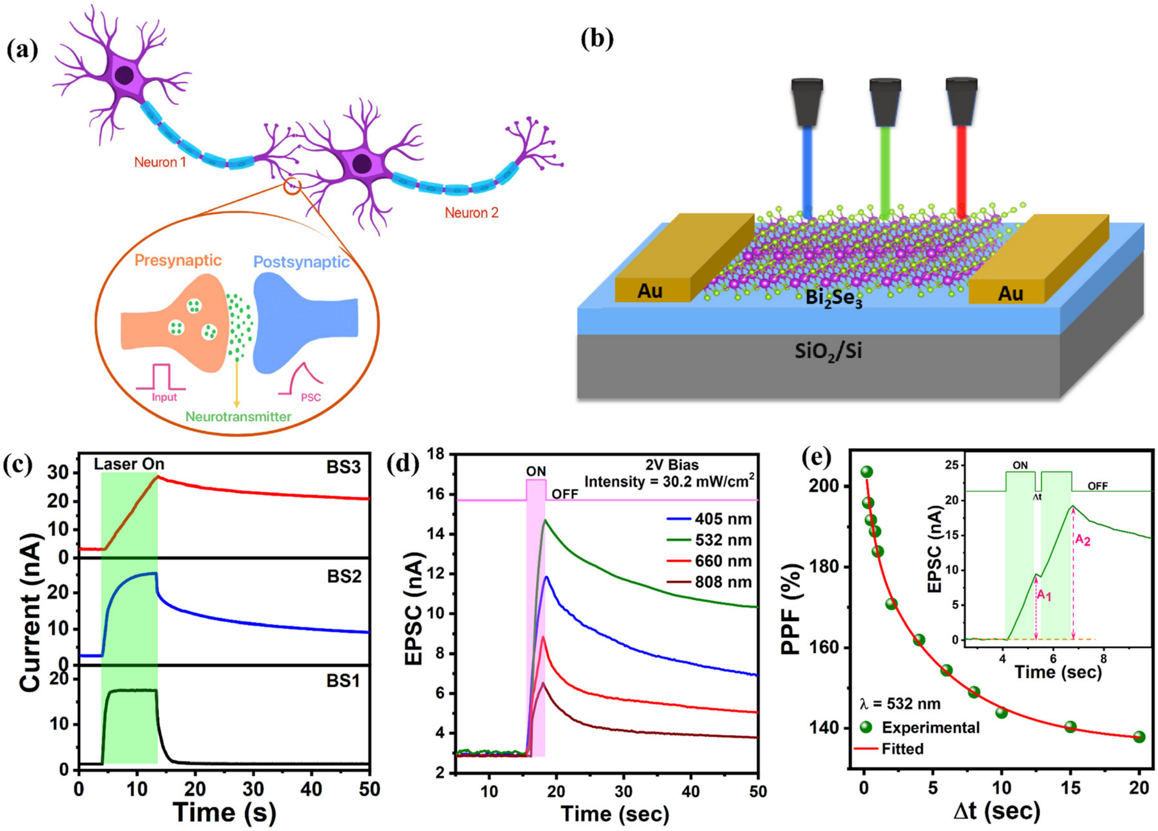

Fig. 3 (a) Schematic diagram of the functionalities of biological synapses. (b) Schematic of the Bi_2Se_3-based optoelectronic synapse device. (c) The transient optical response of the devices made using BS1, BS2, and BS3 films subjected to a single light pulse of 10 s using 532 nm laser with an intensity of 30.2 mW cm^{-2} at 2 V. (d) The change in the EPSC (photocurrent response) of the BS3 device with a single laser pulse of different wavelengths with 30.2 mW cm^{-2} intensity. (e) PPF index of the BS3 device as a function of optical pulse interval (Δt) with a light intensity of 30.2 mW cm^{-2} and a pulse width of 1 s. The red solid line is fitted by an exponential function. The inset shows that the EPSC is triggered by a pair of optical pulses (532 nm, 30.2 mW cm^{-2}, 1 s) with an interval time of 200 ms.

BS3 samples is attributed to the desired persistent photoconductivity (PPC) effect, which is crucial in mimicking biological synaptic plasticity. As the growth temperature increases, the amount of Se vacancies increases, and thus, the PPC effect is more prominent in BS3, which can be a very good candidate for optoelectronic synapse devices. Further testing and characterization are needed at this juncture for the measurement of OES device performance parameters, and the discussion below is for the BS3 sample grown at 335 °C (precursor temperature at 600 °C), as this sample shows the most effective memory retention and highest current as seen in Fig. 3c.

Fig. 3(d) presents the transient optical response of the OES device (BS3 sample) subjected to light pulses of 2 s of various wavelengths with an intensity of 30.2 mW cm^{-2}. The peak EPSC values of the device at 2 V bias under 405 nm, 532 nm, 660 nm and 808 nm wavelength laser pulses are 11.86, 14.71, 8.85 and 6.65 nA, respectively, indicating its potential in broadband optoelectronic synapse applications. The device produced the highest photocurrent under 532 nm light, consistent with its high absorption at this wavelength as revealed by the UV-vis absorption spectrum shown in Fig. 2(d). Consequently, 532 nm light was primarily used as the input signal in the subsequent optical performance evaluations.

PPF is a notable characteristic of biological synapses, indicating that the EPSC induced by the second pulse exceeds that produced by the first pulse. This effect can be influenced by the interval between the two light pulses. As illustrated in the inset of Fig. 3(e), the amplitude of the second EPSC spike is greater than that of the first. The PPF index of the artificial synapse is defined by:[23]

$$\mathrm{PPF} = \frac{A_2}{A_1} \times 100\% \tag{3}$$

where A_1 and A_2 denote the magnitude of the first and second EPSC, respectively, after subtracting the initial dark current. In biological synapses, the amount of neurotransmitter released in synapses is closely linked to the quantity of calcium ions (Ca^{2+}).[52] Facilitation primarily occurs due to the low level of residual Ca^{2+} in the pre-synapse after the first action potential. When the next action potential arrives, the remaining Ca^{2+} contributes to an increased release of neurotransmitters. The PPF in our device can be attributed to the electron-trapping effect; some photogenerated charge carriers were trapped following the first pulse, resulting in a metastable current. The second pulse generated additional charge carriers, causing the second EPSC spike to be higher than the first one. The PPF depends highly on the time interval (Δt) between two consecutive pulses shown in Fig. 3(e). The maximum PPF index here was 203.6% at a 532 nm wavelength with a Δt of 200 ms. This measurement was repeated three times and the results were similar as seen in Fig. S10 (ESI†). The average maximum PPF index of the device from the three trials is 201.7%. Increasing the time interval to 20 s decreased the PPF index to 137.8%. The decrease in the PPF index might be attributed to the trapping and dissipation of electrons during extended interval times. The decay curve of the PPF index with interval time can be fitted with the following double-exponential function:[53]

$$\mathrm{PPF} = 1 + C_1 \exp\left(\frac{-\Delta t}{\tau_1}\right) + C_2 \exp\left(\frac{-\Delta t}{\tau_2}\right) \tag{4}$$

where C_1 (C_2) and τ_1 (τ_2) are the initial facilitation magnitude and characteristic relaxation time of the rapid (slow) decay, respectively. According to the fitting results, τ_1 and τ_2 were 0.7 and 5.9 s, respectively. This is quantitatively close to the time scales of biological synapses.[12]

The energy (E) consumed per synaptic event for a single pulse is calculated, as has been done in previous studies,[20,45] using the formula $E = I \times V \times \Delta t$, where I represents the photocurrent, Δt denotes the pulse duration, and V is the voltage applied to the device. This spike energy indicates the energy cost for each synaptic event. In the context of low-power neuromorphic devices, minimizing the energy per spike is essential for creating efficient and scalable systems that emulate biological neural networks. Estimation of the lowest power consumption requires applying the smallest voltage possible; here $V = 0.01$ V, below which there was no measurable signal under light illumination. As seen in Fig. S11 (ESI†), our OES device uses a very low energy per spike of 9.2 fJ for 200 ms, and as the pulse duration grows, so does the energy consumption. This low value here is approximately similar to the energy consumption of the human brain and within the 1–100 fJ range known for biological systems.

The human memory function is generally categorized into short-term memory (STM) and long-term memory (LTM) based on the retention time. Atkinson and Shiffrin suggested that the process of rehearsal learning aids in consolidating memories within the human brain.[46] Fig. 4(a) illustrates that incoming information is promptly encoded and stored in the hippocampus as STM. Subsequently, STM is either converted into LTM through continuous rehearsal of the stimuli or forgotten altogether. Our OES device can likewise facilitate such conversion by changing the intensity, number, frequency and duration of optical pulses. Here, these four quantities were treated as learning intensity, number, frequency and time. As shown in Fig. 4(b), increasing the intensity of optical pulses from 10.09 to 48.45 mW cm^{-2} resulted in a larger EPSC and a longer retention time, indicating the transformation of STM into LTM. The optical pulse duration, frequency, and number of pulses also have a similar influence on the learning and forgetting behaviours of the synaptic device, as seen in Fig. 4(c)–(e), respectively. For an understanding of the retention time, we define the memory retention percentage (M_t) as the normalized time-dependent current decay of the final EPSC of the device:[17]

$$M_t = \frac{I_t - I_{\mathrm{dark}}}{I_{\mathrm{Max}} - I_{\mathrm{dark}}} \times 100\% \tag{5}$$

where I_t is the EPSC changing with time, I_{dark} is the EPSC without any light and I_{Max} is the final EPSC. M_t can be fitted by using the well-known Kohlrausch function:[17]

$$M_t = A \times \exp\left[-\left(\frac{t}{\tau}\right)^{\beta}\right] \tag{6}$$

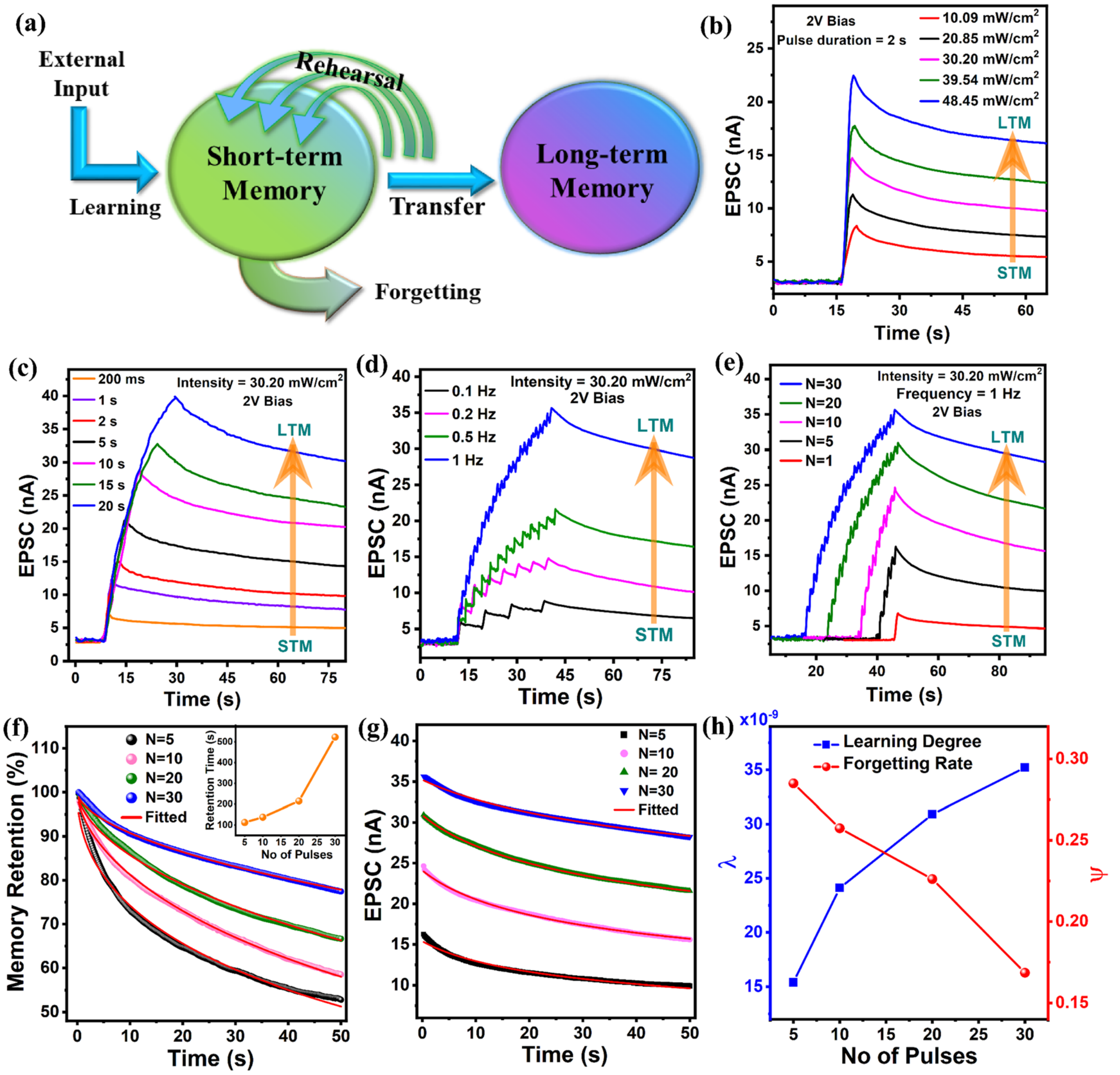

Fig. 4 (a) Schematic diagram illustrating short-term and long-term memory phenomena. The transition of STM to LTM at 2 V bias by increasing (b) the light intensity (532 nm, 2 s), (c) pulse duration (532 nm, 30.2 mW cm^{-2}), (d) pulse frequency (532 nm, 30.2 mW cm^{-2}) and (e) number of pulses (532 nm, 30.2 mW cm^{-2}, 1 Hz). (f) Decay of the normalized memory retention change after stimulation by different pulse numbers. The solid red line is the fitted curve by the Kohlrausch function. The inset shows the change in the retention time with the pulse number. (g) Decay of the EPSC after stimulation by different pulse numbers. The solid red line is the fitted curve by the Wickelgren power-law. (h) The change in learning degree (λ) and forgetting parameter (ψ) with different numbers of pulses.

where A is the constant, τ is the characteristic retention time and β is the stretch index ranging between 0 and 1. The fitting of the decay of the EPSC after fitting the M_t is shown in Fig. 4(f). The values of τ for the number of pulses of N = 5, 10, 20, and 30 are found to be ~112, 137.6, 214.9, and 523.1 s, respectively, as shown in the inset of Fig. 4(f). The increase of τ with the number of spikes confirms the STM-to-LTM transition of the Bi_2Se_3-based OES device. The same trends for the dependence of τ on the pulse intensity, duration, and frequency were observed for the device, as shown in Fig. S12a, d and g (ESI†).

The STM-to-LTM transition can be seen from another aspect proposed by Wickelgren, which is considered a suitable model to describe the biological forgetting law:[53]

$$I = \lambda \times (1 + \beta \times t)^{-\psi} \quad (7)$$

where I is the EPSC, t is the decay time, λ is the state of long-term memory at t = 0 (degree of learning), β is the scale parameter and ψ is the forgetting rate. The current curves (EPSC) for a different number of pulses are well-fitted by the Wickelgren power-law model with different forgetting rates (Fig. 4(g)). Fig. 4(h) shows the pulse-number-dependent memory ability and forgetting rate, where ψ decreases significantly with the spike number increase, but λ shows completely opposite behavior. The deeper learning (higher λ) can be caused by repetitive learning; in other words, repetitive learning can build up a more stable state, which also decreases the forgetting ability (lower ψ). The same trends for the pulsing duration, intensity and frequency were observed for the device as shown in Fig. S12b, c, e, f, h and i (ESI†). The values of the parameters (τ, λ and ψ) confirming STM to LTM transition for all four cases (different intensity, pulse duration, the number of pulses and pulse frequency) are summarized in Table S1 (ESI†).

The impact of growth temperature on the evolution of the PPC effect and subsequent device performance is of interest and for that reason, we also examined the BS2 sample. Fig. S13a–c (ESI†) shows the increment in EPSC for the BS2 sample with increasing pulse duration, light intensity and frequency of the light pulse under 532 nm laser illumination, indicating the transformation of STM into LTM just like the behavior of the BS3 device, although the memory retention here is low as expected. The maximum PPF index of the device is found to be 127.6% at a Δt of 200 ms, as seen in Fig. S13d (ESI†). Note that a similar analysis of the BS1 sample grown at a lower temperature is not needed since it behaves like a photodetector.

DFT results

The PPC effect due to the Se vacancies in the Bi_2Se_3 thin film is vital for the functioning of the OES device as intended. The effect of Se vacancies on the band structure and trap states of Bi_2Se_3 is further investigated using first-principles calculations. Fig. 5(a) shows the band diagram of the 4-layer Bi_2Se_3 based on DFT simulation. The band gap is found to be 0.47 eV, which aligns with previous reports.[50] Multiple trap states (deep and shallow traps) are created in the band structure of Bi_2Se_3 after introducing Se vacancies, as illustrated in Fig. 5(b). The corresponding total density of states (DOS) curves are shown in Fig. 5(c) Detailed atomic structures of 4-layer Bi_2Se_3 and Bi_2Se_3 with Se vacancies are shown in Fig. S14a and b (ESI†), respectively. The electronic band structure obtained from this DFT analysis reveals the emergence of trap states within the forbidden energy gap of Bi_2Se_3 when Se vacancies are introduced. This is further supported by the corresponding DOS plot. These trap states play a crucial role in the synaptic performance of the devices, as charge carriers excited to the conduction band can temporarily reside in these intermediate energy states, contributing to persistent photoconductivity. The DFT results thus confirm that the formation of these intermediate trap states is a direct consequence of atomic Se vacancies, which enhance the synaptic response by reducing the recombination rate.

Mechanism

We present an energy band diagram of Bi_2Se_3 with Au electrodes to gain deeper insight into the mechanism underlying the optoelectronic synaptic behavior, which results from the combined effects of photoresponse and persistent photoconductivity. The energy levels of the Bi_2Se_3 film (BS3) are analyzed using ultraviolet photoelectron spectroscopy (UPS), with the corresponding spectra and calculation details shown in Fig. S15 (ESI†). The maximum valence band energy is estimated to be 5.08 eV, while the Fermi level of Bi_2Se_3 is calculated as 4.42 eV. The work function of Au is 5.1 eV. Fig. S16 (ESI†) illustrates the band diagram of Bi_2Se_3 in conjunction with the Au electrodes. When a laser pulse excites the system, electrons are promoted

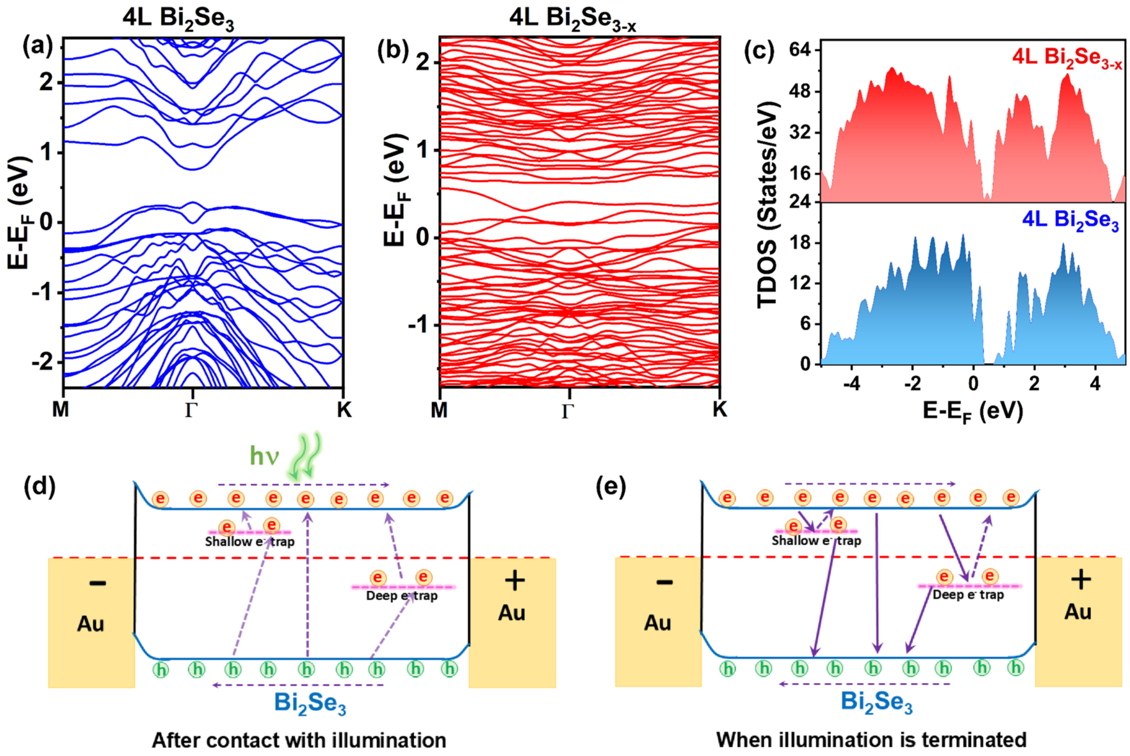

Fig. 5 (a) Energy band diagram of 4-layer Bi_2Se_3 obtained from DFT calculations. (b) Band diagram of 4-layer Bi_2Se_3 with Se vacancies. (c) Total density of states (TDOS) obtained for the pristine 4L Bi_2Se_3 (lower) and Se vacancy-induced Bi_2Se_3 (upper). (d) Schematic of the energy band structure of Bi_2Se_3 along with the Au electrodes under illumination showing charge separation and trapping. (e) Schematic of the energy band structure of Bi_2Se_3 along with the Au electrodes when illumination is terminated showing charge trapping and recombination.

from the valence band to the conduction band (Fig. 5(d)). These conduction band electrons migrate in a specific direction under an applied bias, while the holes in the valence band move in the opposite direction, generating a photocurrent in the circuit. However, some electrons are captured before reaching the conduction band due to the presence of trap states within the bandgap (primarily caused by Se vacancies, which was verified by the DFT results). These trapped electrons can later be released upon gaining thermal energy or additional photon energy, allowing them to transition into the conduction band. This delayed release prolongs the carrier lifetime, leading to a longer rise time in the photoconductivity response. After the illumination is turned off, the photoexcited electrons in the conduction band would quickly recombine with holes in the valence band in an ideal Bi_2Se_3 film (without defects) shown in Fig. 5(e). However, some electrons remain trapped in defect states in a defective Bi_2Se_3 film and require thermal excitation to return to the conduction band before recombining with holes. This mechanism extends the decay time (or fall time) of the photocurrent.

The decay time of the photoconductor is given by the equation: $\tau_{\text{decay}} = \tau_r + \tau_t(1 + \rho)$, where τ_r is the direct recombination time (fast process), τ_t is the de-trapping time (the time required for carriers to escape from trap states *via* thermal excitation, which is a slow process), and ρ represents the probability of an electron/hole being re-trapped before recombination.[54] The de-trapping time (τ_t) depends on the energy barrier ΔE between the trap level and the conduction/valence band, as described by the thermal activation relation: $\tau_t = \tau_0 \exp(\Delta E/kT)$.[21] Here τ_0 is the characteristic time constant under stable conditions, k is the Boltzmann constant, and T is the temperature. Consequently, the relaxation process is significantly extended due to the presence of localized trap states induced by Se vacancies in Bi_2Se_3, which play a crucial role in the persistent photoconductivity behavior.

Human perceptual learning simulation

The "learning–forgetting–relearning" is a typical characteristic of human perceptual learning. This behavior has been imitated by the Bi_2Se_3 OES device using two sequences of successive light pulses with an interval of 200 ms, as shown in Fig. 6(a). The first set of pulses (57 pulses) are shined on the device to imitate the first learning process of the brain, where the synaptic current EPSC increases from 28.9 nA to 40.1 nA. After removal of the light stimuli, the EPSC undergoes spontaneous decay, similar to how our brain gradually forgets information. In the second learning process, achieving the same current level as in the first learning process requires only 36 pulses,

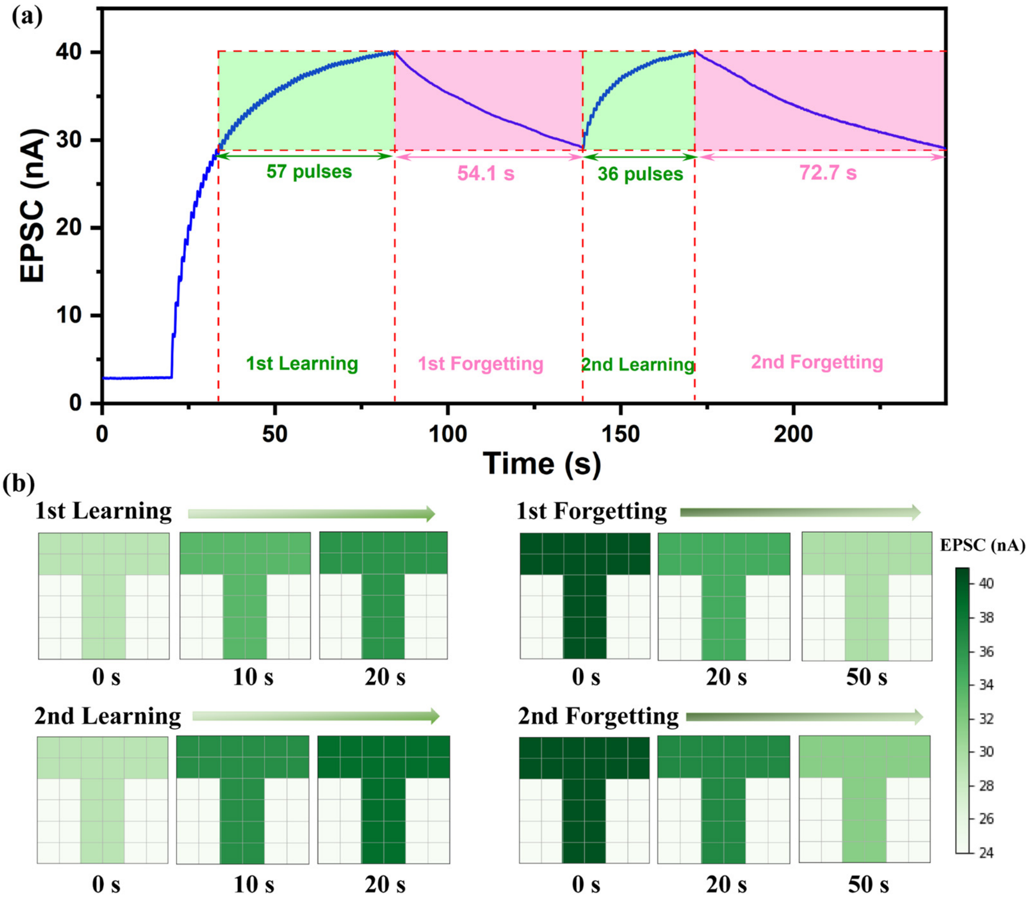

Fig. 6 (a) The learning–forgetting–relearning behavior of the OES device showing that the 2nd learning is faster than the 1st learning and the 2nd forgetting is slower than the 1st one, similar to our brain. (b) Illustration of the visual memory function in a 6 × 6 array.

demonstrating that less time is needed for relearning. This is similar to how people generally learn more rapidly during the second relearning process. Furthermore, the observed current decay in the second forgetting process (72.7 seconds) is slower than in the first forgetting process (54.1 seconds); this reflects the improved long-term memory retention in humans after multiple learning experiences. Although the mechanism of electron de-trapping remains the same in both forgetting processes, the distribution and density of holes change after the learning–forgetting–relearning cycle. This means that some holes have been firmly occupied by doping electrons before the second forgetting process; then, the altered distribution of the reduced number of holes can cause the slower current decay observed in the second forgetting process. The interesting "learning–forgetting–relearning" behavior verifies that the mimicking of human perceptual learning can be conducted by the synaptic array with a long-term photocurrent response.

Fig. 6(b) shows a visual memory simulation utilizing photoreaction data obtained from the "learning–forgetting–relearning" curve, as depicted in Fig. 6(a). The EPSC is mapped as "*T*" using a 6 × 6 square array, where the bright green and white pixels represent the light and dark currents, respectively. The color contrast of the "*T*" pattern increases with the learning time increasing from 0 to 20 s, demonstrating the human brain's dynamic learning process. After 10 s and 20 s, the color contrast of the pattern is better in the case of 2nd learning than in the 1st learning. On the other hand, the color contrast of the pixels decreases with the increase in forgetting time from 0 to 50 s. The higher color contrast of the pattern indicates that memory retention is more in the 2nd case. We can identify the "*T*" pattern even after 50 s, as the color contrast decreased by only 22%, which suggests strong memory characteristics of the OES device.

MNIST handwritten digit recognition simulation

The MNIST (Modified National Institute of Standards and Technology) handwritten digit recognition task was performed by an artificial neural network (ANN) using the long-term potentiation (LTP) data in order to show the potential of our OES device in neuromorphic computing. Fig. 7(a) displays the

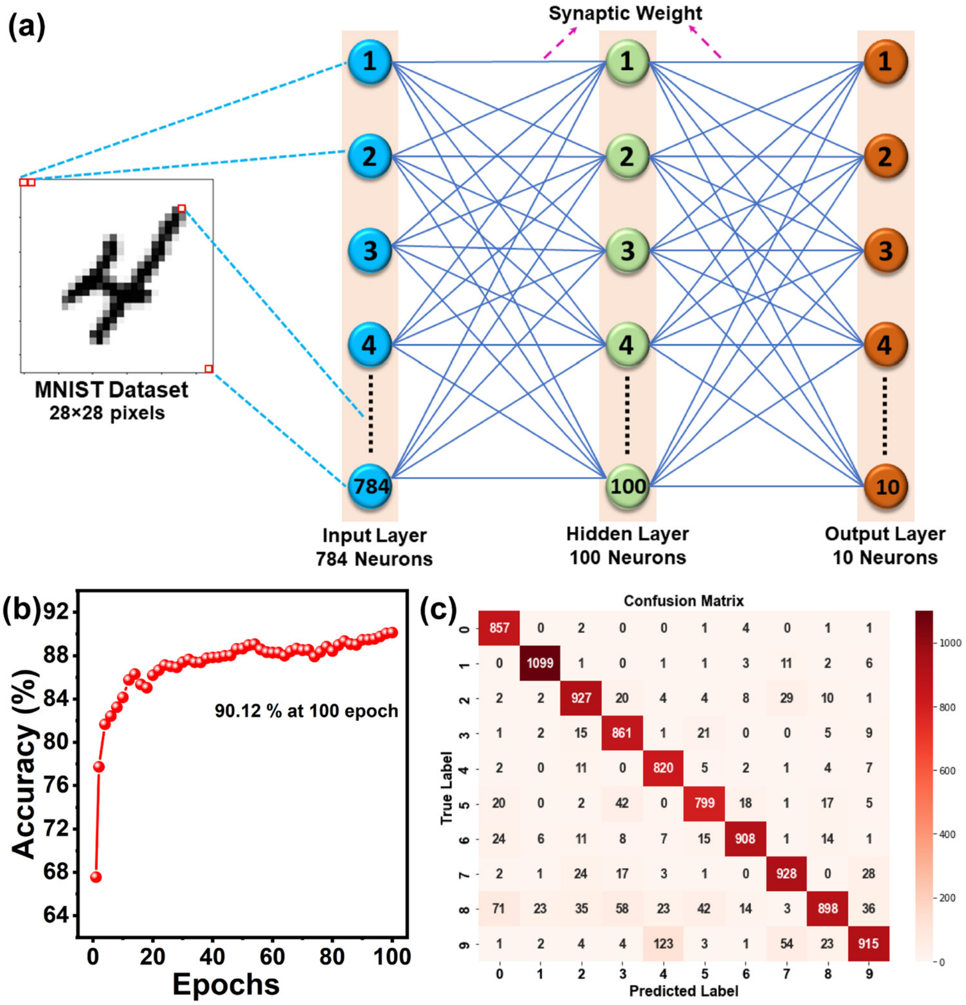

Fig. 7 (a) Schematic of the ANN architecture for MNIST handwritten digit recognition containing 784 input, 100 hidden and 10 output neurons. (b) The accuracy of MNIST digits computed from ANN simulation in every epochs. (c) The confusion matrix of accuracy 90.12% obtained after 100 epochs.

Table 1 Comparison of the performance of 2D material-based OES devices in the literature with our device. Unless noted, all devices are two terminal photoconductors. Δt denotes the light pulse duration

Material	Wavelength, nm	Intensity (mW cm^{-2})	PPF, %	Energy/spike and Δt, ms	Ref.
MoS_2	532	0.21	190	77.6 pJ, 100	16
hBN/MoS_2 transistor	532	50	124	80.0 pJ, —	55
hBN/MoS_2 transistor	470	0.0135	~270	2.52 fJ, 50	56
Violet phosphorus-MoS_2 transistor	473	—	853	0.8 pJ, 200	57
Black phosphorus	280	3	155	3.5 pJ, 100	58
Sb_2Te_3	450	1400	162	—	35
$MoSe_2$	550	1113	108	10.0 fJ, 200	18
$MoSe_2/Bi_2Se_3$	790	1.65	153	0.75 nJ, 10	34
Bi_2O_2Se	532	0.86	160	—	23
ReS_2	450	37	124	12.1 fJ, 200	21
In_2S_3	285	3	169	0.81pJ, —	59
InSe	405	38.9	117	100 fJ, 1	60
Bi_2Se_3	532	30.2	203.6	9.2 fJ, 200	This work

schematic of the ANN architecture containing 784 input, 100 hidden and 10 output neurons. Every input neuron is connected to all the hidden neurons and every hidden neuron is connected to all output neurons by our OES. The ANN was trained first using a back-propagation algorithm with 50 000 images of handwritten digits. Then a MNIST test dataset containing 10 000 images different from the trained images was fed to the ANN to calculate the recognition accuracy of the model. Here, the synaptic weights of the network were presented as the difference between two conductance values, namely $W = G^+ - G^-$. The weight update can be represented by the conductance update of the LTP curve using the equation[7,19]

$$G_{n+1} - G_n = \alpha_p e^{-\beta_p \frac{G_n - G_{\min}}{G_{\max} - G_{\min}}} \tag{8}$$

where G_n and G_{n+1} are the conductance values of one step and the next step and $G_{\max}$ and $G_{\min}$ are the maximum and the minimum values of conductance. Besides, α_p and β_p present the step sizes of the change in conductance and nonlinearity, respectively. Fig. S17a (ESI†) displays the LTP curves, which present the change in conductance value of the device with increasing pulse number. The fitted nonlinearity curves are displayed in Fig. S17b (ESI†), and the α_p and β_p are calculated as 2.0945 nS and 5.8976 nS for image recognition.

The recognition accuracy based on the fitted parameters of the device is presented in Fig. 7(b). After the training process of 100 epochs, the recognition accuracy reached 90.12%, demonstrating the synaptic rapid learning and recognition capabilities of the OES. The confusion matrix of the 90.12% accuracy after the learning is shown in Fig. 7(c). The proposed OES device technology is expected to play an important role in implementing novel neuromorphic computing based on optoelectronic signal processing.

Finally, Table 1 presents a comparison of our results with other 2D material-based OES devices in the literature. The Bi_2Se_3-based device here provides the highest PPF and lowest energy consumption among all two-terminal-based devices, thus offering a compelling candidate for the construction of optoelectronic synaptic devices for the future.

Conclusions

We have developed an optoelectronic synapse using a CVD-grown ultrathin layer of Bi_2Se_3 and investigated key characteristics such as paired-pulse facilitation (PPF), short-term and long-term memory, and learning–relearning behavior. Specifically, we were able to modulate the Se vacancies by varying the growth temperature. Our OES device with a Se-vacancy-rich film displays a very high PPF index of 201.7%, a long retention time of 523.1 s and an ultralow energy consumption of 9.2 fJ per spike. First principles-based calculations confirm the role of Se vacancies in the observed performance of Bi_2Se_3 OES devices. The metrics achieved here are by far the best reported to date, especially PPF and energy consumption per spike, for single material based two-terminal devices. Any exceptions revealing better performance involve complex heterostructures of multiple materials and/or three-terminal transistors. An artificial neural network architecture was simulated using the learning properties of our OES device to successfully realize a high recognition accuracy of 90.12% for MNIST handwritten digital images, which shows the potential of our device in future neuromorphic computing applications. Bi_2Se_3 is a highly important topological insulator that has been explored for a wide range of applications but not for optoelectronic artificial synapses until now. The simplicity of the device, reliable Se vacancy-based mechanism and exceptional results achieved here show the potential of Bi_2Se_3 for this application and pave the way for exploiting this potential in future high-performance neuromorphic computing and other artificial visual perception systems. Future work can include further quantification of defects for the understanding of the influence of various parameters. The defect-dependent mechanism also makes the study of control and manipulation of defects (*i.e.* defect engineering) and identification of avenues for such control besides growth temperature an important aspect in the field of materials science of 2D topological insulators.

Author contributions

SN designed and performed all the experiments, SG performed modeling, MM helped with the analysis of the results and writing the manuscript, and PKG supervised the project and helped with the design of the study, interpretation of the results, and writing the manuscript.

Data availability

The data supporting this article have been included in the manuscript and ESI.†

Conflicts of interest

The authors declare no conflicts of interest.

Acknowledgements

This work was supported by the MEITY (5(1)/2022-NANO) and SERB (CRG/2021/006397) of the Government of India. The authors acknowledge the Central Instrument Facility of the Indian Institute of Technology Guwahati for access to various instruments. SN acknowledges financial support from the Prime Minister Research Fellowship (PMRF). The authors thank Prof. Merlyne De Souza of the University of Sheffield (UK) for her critical review of the manuscript and feedback.

References

1 L. Mennel, J. Symonowicz, S. Wachter, D. K. Polyushkin, A. J. Molina-Mendoza and T. Mueller, Ultrafast Machine Vision with 2D Material Neural Network Image Sensors, *Nature*, 2020, **579**(7797), 62–66, DOI: 10.1038/s41586-020-2038-x.

2 H. Haick and N. Tang, Artificial Intelligence in Medical Sensors for Clinical Decisions, *ACS Nano*, 2021, **15**(3), 3557–3567, DOI: 10.1021/acsnano.1c00085.

3 K. He, Y. Liu, J. Yu, X. Guo, M. Wang, L. Zhang, C. Wan, T. Wang, C. Zhou and X. Chen, Artificial Neural Pathway Based on a Memristor Synapse for Optically Mediated Motion Learning, *ACS Nano*, 2022, **16**(6), 9691–9700, DOI: 10.1021/acsnano.2c03100.

4 P. A. Merolla, J. V. Arthur, R. Alvarez-Icaza, A. S. Cassidy, J. Sawada, F. Akopyan, B. L. Jackson, N. Imam, C. Guo, Y. Nakamura, B. Brezzo, I. Vo, S. K. Esser, R. Appuswamy, B. Taba, A. Amir, M. D. Flickner, W. P. Risk, R. Manohar and D. S. Modha, A Million Spiking-Neuron Integrated Circuit with a Scalable Communication Network and Interface, *Science*, 2014, **345**(6197), 668–673, DOI: 10.1126/science.1254642.

5 S. Dai, Y. Zhao, Y. Wang, J. Zhang, L. Fang, S. Jin, Y. Shao and J. Huang, Recent Advances in Transistor-Based Artificial Synapses, *Adv. Funct. Mater.*, 2019, **29**(42), 1903700, DOI: 10.1002/adfm.201903700.

6 A. Gaurav, X. Song, S. Manhas, A. Gilra, E. Vasilaki, P. Roy and M. M. De Souza, Reservoir Computing for Temporal Data Classification Using a Dynamic Solid Electrolyte ZnO Thin Film Transistor, *Front. Electron.*, 2022, **3**, 1–9, DOI: 10.3389/felec.2022.869013.

7 P. Zhao, X. Peng, M. Cui, Y. Li, C. Jiang, C. Luo, B. Tian, H. Lin, H. Peng and C. G. Duan, Multifunctional Two-Terminal Optoelectronic Synapse Based on an Organic Semiconductor Film, *ACS Appl. Polym. Mater.*, 2023, **5**(10), 8764–8773, DOI: 10.1021/acsapm.3c02012.

8 Q. Wu, J. Wang, J. Cao, C. Lu, G. Yang, X. Shi, X. Chuai, Y. Gong, Y. Su, Y. Zhao, N. Lu, D. Geng, H. Wang, L. Li and M. Liu, Photoelectric Plasticity in Oxide Thin Film Transistors with Tunable Synaptic Functions, *Adv. Electron. Mater.*, 2018, **4**(12), 1–8, DOI: 10.1002/aelm.201800556.

9 H. Lian, Q. Liao, B. Yang, Y. Zhai, S. T. Han and Y. Zhou, Optoelectronic Synaptic Transistors Based on Upconverting Nanoparticles, *J. Mater. Chem. C*, 2021, **9**(2), 640–648, DOI: 10.1039/d0tc04115g.

10 G. Li, D. Xie, H. Zhong, Z. Zhang, X. Fu, Q. Zhou, Q. Li, H. Ni, J. Wang, E. jia Guo, M. He, C. Wang, G. Yang, K. Jin and C. Ge, Photo-Induced Non-Volatile VO_2 Phase Transition for Neuromorphic Ultraviolet Sensors, *Nat. Commun.*, 2022, **13**(1), 1–9, DOI: 10.1038/s41467-022-29456-5.

11 Y. Wang, Y. Zha, C. Bao, F. Hu, Y. Di, C. Liu, F. Xing, X. Xu, X. Wen, Z. Gan and B. Jia, Monolithic 2D Perovskites Enabled Artificial Photonic Synapses for Neuromorphic Vision Sensors, *Adv. Mater.*, 2024, **2311524**, 1–11, DOI: 10.1002/adma.202311524.

12 H. Tan, Z. Ni, W. Peng, S. Du, X. Liu, S. Zhao, W. Li, Z. Ye, M. Xu, Y. Xu, X. Pi and D. Yang, Broadband Optoelectronic Synaptic Devices Based on Silicon Nanocrystals for Neuromorphic Computing, *Nano Energy*, 2018, **52**, 422–430, DOI: 10.1016/j.nanoen.2018.08.018.

13 W. Xiao, L. Shan, H. Zhang, Y. Fu, Y. Zhao, D. Yang, C. Jiao, G. Sun, Q. Wang and D. He, High Photosensitivity Light-Controlled Planar ZnO Artificial Synapse for Neuromorphic Computing, *Nanoscale*, 2021, **13**(4), 2502–2510, DOI: 10.1039/d0nr08082a.

14 Y. B. Guo, Y. L. Liu, Q. L. Chen and G. Liu, Titanium Oxide-Based Optoelectronic Synapses with Visual Memory Synergistically Adjusted by Internal Emotions and Ambient Illumination, *RSC Adv.*, 2022, **12**(42), 27162–27169, DOI: 10.1039/d2ra02749f.

15 W. Yang, H. Kan, G. Shen and Y. Li, A Network Intrusion Detection System with Broadband WO_{3-x}/WO_{3-x}–Ag/WO_{3-x} Optoelectronic Memristor, *Adv. Funct. Mater.*, 2024, **34**(23), 2312885, DOI: 10.1002/adfm.202312885.

16 M. Huang, W. Ali, L. Yang, J. Huang, C. Yao, Y. Xie, R. Sun, C. Zhu, Y. Tan, X. Liu, S. Li, Z. Li and A. Pan, Multifunctional Optoelectronic Synapses Based on Arrayed MoS_2 Monolayers Emulating Human Association Memory, *Adv. Sci.*, 2023, **10**(16), 2300120, DOI: 10.1002/advs.202300120.

17 Z. D. Luo, X. Xia, M. M. Yang, N. R. Wilson, A. Gruverman and M. Alexe, Artificial Optoelectronic Synapses Based on Ferroelectric Field-Effect Enabled 2D Transition Metal Dichalcogenide Memristive Transistors, *ACS Nano*, 2020, **14**(1), 746–754, DOI: 10.1021/acsnano.9b07687.

18 H. Yang, Y. Hu, X. Zhang, Y. Ding, S. Wang, Z. Su, Y. Shuai and P. Hu, Near-Infrared Optical Synapses Based on Multilayer $MoSe_2$ Moiré Superlattice for Artificial Retina, *Adv.*

Funct. Mater., 2024, **34**(2), 2308149, DOI: 10.1002/adfm.202308149.

19 Z. Guo, J. Liu, X. Han, F. Ma, D. Rong, J. Du, Y. Yang, T. Wang, G. Li, Y. Huang and J. Xing, High-Performance Artificial Synapse Based on CVD-Grown WSe_2 Flakes with Intrinsic Defects, *ACS Appl. Mater. Interfaces*, 2023, **15**(15), 19152–19162, DOI: 10.1021/acsami.3c00417.

20 J. Jiang, W. Xu, Z. Sun, L. Fu, S. Zhang, B. Qin, T. Fan, G. Li, S. Chen, S. Yang, W. Ge, B. Shen and N. Tang, Wavelength-Controlled Photoconductance Polarity Switching via Harnessing Defects in Doped $PdSe_2$ for Artificial Synaptic Features, *Small*, 2024, **20**(13), 2306068, DOI: 10.1002/smll.202306068.

21 Y. Chen, Y. Huang, J. Zeng, Y. Kang, Y. Tan, X. Xie, B. Wei, C. Li, L. Fang and T. Jiang, Energy-Efficient ReS_2-Based Optoelectronic Synapse for 3D Object Reconstruction and Recognition, *ACS Appl. Mater. Interfaces*, 2023, **15**(50), 58631–58642, DOI: 10.1021/acsami.3c14958.

22 S. Mukherjee, D. Dutta, A. Ghosh and E. Koren, Graphene-In_2Se_3 van der Waals Heterojunction Neuristor for Optical In-Memory Bimodal Operation, *ACS Nano*, 2023, **17**(22), 22287–22298, DOI: 10.1021/acsnano.3c03820.

23 X. Ren, X. He, X. Li, Y. Li, F. Gao, J. Zhang and P. Hu, An Optical Artificial Synapse Based on Single-Crystal Se-Vacancy Bi_2O_2Se, *Adv. Opt. Mater.*, 2024, **12**(14), 2302852, DOI: 10.1002/adom.202302852.

24 Y. Wang, Z. Lv, J. Chen, Z. Wang, Y. Zhou, L. Zhou, X. Chen and S.-T. Han, Photonic Synapses Based on Inorganic Perovskite Quantum Dots for Neuromorphic Computing, *Adv. Mater.*, 2018, **30**(38), 1802883, DOI: 10.1002/adma.201802883.

25 P. Guo, J. Zhang, D. Liu, R. Wang, L. Li, L. Tian and J. Huang, Optoelectronic Synaptic Transistors Based on Solution-Processable Organic Semiconductors and $CsPbCl_3$ Quantum Dots for Visual Nociceptor Simulation and Neuromorphic Computing, *ACS Appl. Mater. Interfaces*, 2023, **15**(44), 51483–51491, DOI: 10.1021/acsami.3c09355.

26 R. Li, Y. Dong, F. Qian, Y. Xie, X. Chen, Q. Zhang, Z. Yue and M. Gu, $CsPbBr_3$/Graphene Nanowall Artificial Optoelectronic Synapses for Controllable Perceptual Learning, *PhotoniX*, 2023, **4**, 4, DOI: 10.1186/s43074-023-00082-8.

27 H. Chen, N. Qin, Z. Ren, Y. Fan, Q. Congyao, C. Liu, W. Peng, B. Huang and T. Guo, MXene-Based Optoelectronic Synaptic Transistors Utilize Attentional Mechanisms to Achieve Hierarchical Responses, *J. Mater. Chem. C*, 2024, **12**(20), 7197–7205, DOI: 10.1039/d4tc00473f.

28 Y. Zhang, K. He, C. Z. Chang, C. L. Song, L. L. Wang, X. Chen, J. F. Jia, Z. Fang, X. Dai, W. Y. Shan, S. Q. Shen, Q. Niu, X. L. Qi, S. C. Zhang, X. C. Ma and Q. K. Xue, Crossover of the Three-Dimensional Topological Insulator Bi_2Se_3 to the Two-Dimensional Limit, *Nat. Phys.*, 2010, **6**(8), 584–588, DOI: 10.1038/nphys1689.

29 H. Peng, W. Dang, J. Cao, Y. Chen, D. Wu, W. Zheng, H. Li, Z. X. Shen and Z. Liu, Topological Insulator Nanostructures for Near-Infrared Transparent Flexible Electrodes, *Nat. Chem.*, 2012, **4**(4), 281–286, DOI: 10.1038/nchem.1277.

30 L. He, F. Xiu, X. Yu, M. Teague, W. Jiang, Y. Fan, X. Kou, M. Lang, Y. Wang, G. Huang, N. C. Yeh and K. L. Wang, Surface-Dominated Conduction in a 6 nm Thick Bi_2Se_3 Thin Film, *Nano Lett.*, 2012, **12**(3), 1486–1490, DOI: 10.1021/nl204234j.

31 F. K. Wang, S. J. Yang and T. Y. Zhai, 2D Bi_2Se_3 Materials for Optoelectronics, *iScience*, 2021, **24**(11), 1–17, DOI: 10.1016/j.isci.2021.103291.

32 S. Nandi, K. Ghosh, M. Meyyappan and P. K. Giri, 2D MXene Electrode-Enabled High-Performance Broadband Photodetector Based on a CVD-Grown 2D Bi_2Se_3 Ultrathin Film on Silicon, *ACS Appl. Electron. Mater.*, 2023, **5**(12), 6985–6995, DOI: 10.1021/acsaelm.3c01363.

33 L. A. Walsh, A. J. Green, R. Addou, W. Nolting, C. R. Cormier, A. T. Barton, T. R. Mowll, R. Yue, N. Lu, J. Kim, M. J. Kim, V. P. Labella, C. A. Ventrice, S. McDonnell, W. G. Vandenberghe, R. M. Wallace, A. Diebold and C. L. Hinkle, Fermi Level Manipulation through Native Doping in the Topological Insulator Bi_2Se_3, *ACS Nano*, 2018, **12**(6), 6310–6318, DOI: 10.1021/acsnano.8b03414.

34 Y. Wang, J. Yang, W. Ye, D. She, J. Chen, Z. Lv, V. A. L. Roy, H. Li, K. Zhou, Q. Yang, Y. Zhou and S.-T. Han, Near-Infrared-Irradiation-Mediated Synaptic Behavior from Tunable Charge-Trapping Dynamics, *Adv. Electron. Mater.*, 2020, **6**(2), 1900765, DOI: 10.1002/aelm.201900765.

35 Z. Wan, Q. Zhang, F. Hu, Y. Dong, R. Li, L. Hu, Y. Xie, Z. Yue, X. Chen and M. Gu, Topological Insulator Optoelectronic Synapses for High-Accuracy Binary Image Recognition Using Recurrent Neural Networks, *Adv. Opt. Mater.*, 2023, **11**(2), 2201852, DOI: 10.1002/adom.202201852.

36 J. Guo, J. Huang, S. Gu, L. Lin, Y. Zhang, X. Wang, Y. Liu, T. Gong, Y. Lin, B. Yu, W. Huang and X. Zhang, Optoelectronic Synapse Enabled by Defect Engineering of Tellurene for Neuromorphic Computing, *IEEE Electron Device Lett.*, 2024, **46**(1), 68–71, DOI: 10.1109/LED.2024.3498106.

37 P. Giannozzi, S. Baroni, N. Bonini, M. Calandra, R. Car, C. Cavazzoni, D. Ceresoli, G. L. Chiarotti, M. Cococcioni, I. Dabo, A. D. Corso, S. de Gironcoli, S. Fabris, G. Fratesi, R. Gebauer, U. Gerstmann, C. Gougoussis, A. Kokalj, M. Lazzeri, L. Martin-Samos, N. Marzari, F. Mauri, R. Mazzarello, S. Paolini, A. Pasquarello, L. Paulatto, C. Sbraccia, S. Scandolo, G. Sclauzero, A. P. Seitsonen, A. Smogunov, P. Umari and R. M. Wentzcovitch, QUANTUM ESPRESSO: A Modular and Open-Source Software Project for Quantum Simulations of Materials, *J. Phys.: Condens. Matter*, 2009, **21**(39), 395502, DOI: 10.1088/0953-8984/21/39/395502.

38 R. G. Parr, Density Functional Theory, *Annu. Rev. Phys. Chem.*, 1983, **34**, 631–656, DOI: 10.1146/annurev.pc.34.100183.003215.

39 P. E. Blöchl, Projector Augmented-Wave Method, *Phys. Rev. B: Condens. Matter Mater. Phys.*, 1994, **50**(24), 17953–17979, DOI: 10.1103/PhysRevB.50.17953.

40 J. P. Perdew, K. Burke and M. Ernzerhof, Generalized Gradient Approximation Made Simple, *Phys. Rev. Lett.*, 1996, **77**(18), 3865–3868, DOI: 10.1103/PhysRevLett.77.3865.

41 S. Gautam, V. Aggarwal, B. Singh, V. P. S. Awana, R. Ganesan and S. S. Kushvaha, Signature of Weak-Antilocalization in Sputtered Topological Insulator Bi_2Se_3 Thin Films with Varying Thickness, *Sci. Rep.*, 2022, **12**(1), 1–10, DOI: **10.1038/s41598-022-13600-8**.

42 Z. Lin, W. Zhang, J. Peng, Q. Li, Z. Liang, G. Wang, J. Wang, G. Wang, Z. Huang and S. Huang, Synergistic Regulation of Polyselenide Dissolution and Na-Ion Diffusion of Se-Vacancy-Rich Bismuth Selenide toward Ultrafast and Durable Sodium-Ion Batteries, *Adv. Energy Mater.*, 2024, **46**(14), 2402110, DOI: **10.1002/aenm.202402110**.

43 S. Hu, X. Huang, L. Zhang, G. Li, S. Chen, J. Zhang and X. Liu, Vacancy-Defect Topological Insulators Bi_2Te_{3-x} Embedded in N and B Co-Doped 1D Carbon Nanorods Using Ionic Liquid Dopants for Kinetics-Enhanced Li–S Batteries, *Adv. Funct. Mater.*, 2023, **33**(20), 2214161, DOI: **10.1002/adfm.202214161**.

44 H. Yan, S. Lin, R. Zhang, H. Li, B. Fu, J. Liu, L. Liu, S. Kunsági-Máté and Y. An, Facile Synthesis of High-Crystalline Bi_2Se_3 Nanoribbons without Se Vacancies and Their Properties, *J. Mater. Sci.*, 2020, **55**(12), 5145–5155, DOI: **10.1007/s10853-020-04354-7**.

45 H. Zhang, X. Zhang, C. Liu, S. T. Lee and J. Jie, High-Responsivity, High-Detectivity, Ultrafast Topological Insulator Bi_2Se_3/Silicon Heterostructure Broadband Photodetectors, *ACS Nano*, 2016, **10**(5), 5113–5122, DOI: **10.1021/acsnano.6b00272**.

46 P. Shen, X. Li, Y. Luo, Y. Guo, X. Zhao and K. Chu, High-Efficiency N_2 Electroreduction Enabled by Se-Vacancy-Rich WSe_{2-x} in Water-in-Salt Electrolytes, *ACS Nano*, 2022, **16**(5), 7915–7925, DOI: **10.1021/acsnano.2c00596**.

47 F. Liu, M. Liu, A. Liu, C. Yang, C. Chen, C. Zhang, D. Bi and B. Man, The Effect of Temperature on Bi_2Se_3 Nanostructures Synthesized via Chemical Vapor Deposition, *J. Mater. Sci.: Mater. Electron.*, 2015, **26**(6), 3881–3886, DOI: **10.1007/s10854-015-2915-5**.

48 V. A. Golyashov, K. A. Kokh, S. V. Makarenko, K. N. Romanyuk, I. P. Prosvirin, A. V. Kalinkin, O. E. Tereshchenko, A. S. Kozhukhov, D. V. Sheglov, S. V. Eremeev, S. D. Borisova and E. V. Chulkov, Inertness and Degradation of (0001) Surface of Bi_2Se_3 Topological Insulator, *J. Appl. Phys.*, 2012, **112**(11), 113702, DOI: **10.1063/1.4767458**.

49 A. K. Mia, M. Meyyappan and P. K. Giri, Asymmetric Contact-Induced Selective Doping of CVD-Grown Bilayer WS_2 and Its Application in High-Performance Photodetection with an Ultralow Dark Current, *Nanoscale*, 2024, **16**(17), 8583–8596, DOI: **10.1039/d3nr06118c**.

50 S. K. Das and P. Padhan, Surface-Induced Enhanced Band Gap in the (0001) Surface of Bi_2Se_3 Nanocrystals: Impacts on the Topological Effect, *ACS Appl. Nano Mater.*, 2020, **3**(1), 274–282, DOI: **10.1021/acsanm.9b01941**.

51 L. Sun, Z. Lin, J. Peng, J. Weng, Y. Huang and Z. Luo, Preparation of Few-Layer Bismuth Selenide by Liquid-Phase-Exfoliation and Its Optical Absorption Properties, *Sci. Rep.*, 2014, **4**, 1–9, DOI: **10.1038/srep04794**.

52 T. Chen, X. Wang, D. Hao, S. Dai, Q. Ou, J. Zhang and J. Huang, Photonic Synapses with Ultra-Low Energy Consumption Based on Vertical Organic Field-Effect Transistors, *Adv. Opt. Mater.*, 2021, **9**(8), 2002030, DOI: **10.1002/adom.202002030**.

53 S. E. Ng, J. Yang, R. A. John and N. Mathews, Adaptive Latent Inhibition in Associatively Responsive Optoelectronic Synapse, *Adv. Funct. Mater.*, 2021, **31**(28), 1–12, DOI: **10.1002/adfm.202100807**.

54 J. Jiang, C. Ling, T. Xu, W. Wang, X. Niu, A. Zafar, Z. Yan, X. Wang, Y. You, L. Sun, J. Lu, J. Wang and Z. Ni, Defect Engineering for Modulating the Trap States in 2D Photoconductors, *Adv. Mater.*, 2018, **30**(40), 1804332, DOI: **10.1002/adma.201804332**.

55 S. Wang, X. Hou, L. Liu, J. Li, Y. Shan, S. Wu, D. W. Zhang and P. Zhou, A Photoelectric-Stimulated MoS_2 Transistor for Neuromorphic Engineering, *Research*, 2019, 2019, DOI: **10.34133/2019/1618798**.

56 Y. Sun, M. Li, Y. Ding, H. Wang, H. Wang, Z. Chen and D. Xie, Programmable Van-Der-Waals Heterostructure-Enabled Optoelectronic Synaptic Floating-Gate Transistors with Ultra-Low Energy Consumption, *InfoMat*, 2022, **4**(10), e12317, DOI: **10.1002/inf2.12317**.

57 X. Liu, S. Wang, Z. Di, H. Wu, C. Liu and P. Zhou, An Optoelectronic Synapse Based on Two-Dimensional Violet Phosphorus Heterostructure, *Adv. Sci.*, 2023, **10**(22), 2301851, DOI: **10.1002/advs.202301851**.

58 T. Ahmed, S. Kuriakose, E. L. H. Mayes, R. Ramanathan, V. Bansal, M. Bhaskaran, S. Sriram and S. Walia, Optically Stimulated Artificial Synapse Based on Layered Black Phosphorus, *Small*, 2019, **15**(22), 1900966, DOI: **10.1002/smll.201900966**.

59 T. Ahmed, A. Jannat, V. Krishnamurthi, T. Aung, A. Mazumder, A. Zavabeti, N. Syed, T. Daeneke, J. Z. Ou, A. Al-Hourani and S. Walia, Atomically Thin Synaptic Devices for Optoelectronic Neuromorphic Vision, *Adv. Mater. Technol.*, 2023, **8**(9), 2201772, DOI: **10.1002/admt.202201772**.

60 X. Wang, X. Zhou, A. Cui, M. Deng, X. Xu, L. Xu, Y. Ye, K. Jiang, L. Shang, L. Zhu, J. Zhang, Y. Li, Z. Hu and J. Chu, Flexo-Photoelectronic Effect in n-Type/p-Type Two-Dimensional Semiconductors and a Deriving Light-Stimulated Artificial Synapse, *Mater. Horiz.*, 2021, **8**(7), 1985–1997, DOI: **10.1039/d1mh00024a**.